Atmospheric Environment 338 (2024) 120859

Contents lists available at ScienceDirect

Atmospheric Environment

journal homepage: www.elsevier.com/locate/atmosenv

Gas-liquid interfacial reaction mechanisms of typical small α-dicarbonyls in the neutral and acidic droplets: Implications for secondary organic aerosol formation

Qiuju Shi [a,b], Ruize Ma [a,b], Yongpeng Ji [a,b], Weina Zhang [a,b], Yuemeng Ji [a,b,*], Taicheng An [a,b]

[a] Guangdong Key Laboratory of Environmental Catalysis and Health Risk Control, Guangdong-Hong Kong-Macao Joint Laboratory for Contaminants Exposure and Health, Institute of Environmental Health and Pollution Control, Guangdong University of Technology, Guangzhou, 510006, China
[b] Guangzhou Key Laboratory of Environmental Catalysis and Pollution Control, Key Laboratory for City Cluster Environmental Safety and Green Development of the Ministry of Education, School of Environmental Science and Engineering, Guangdong University of Technology, Guangzhou, 510006, China

HIGHLIGHTS

- Acidic gas-liquid interface exhibits a strong uptake for MG and BA.
- *Trans* Configurations are the favorable configurations at the interface.
- The C=O groups of MG and BA have the preferential orientation at the interface.
- Subsequent interfacial hydration reactions are accelerated at the acidic interface.

GRAPHICAL ABSTRACT

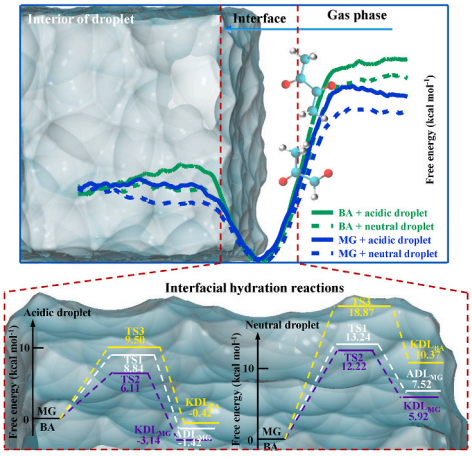

ARTICLE INFO

Keywords:
Gas-liquid interfaces
Small α-dicarbonyls
Uptakes
Hydration reactions
Theoretical simulations

ABSTRACT

Small α-dicarbonyls (SαDs) are well-known as the important precursors of secondary organic aerosol (SOA). Hence, it is imperative to understand the atmospheric chemistry of SαDs to contribute to SOA formation. In this work, we investigated the interfacial chemistry of typical SαDs, including methylglyoxal (MG) and biacetyl (BA) in the neutral and acidic droplets by combined molecular dynamics and quantum chemical calculations. The *trans* configurations of MG and BA are found to be the favorable configurations at the interfaces and are prone to stay at the gas-liquid interface of the acidic droplet. The C=O group exhibits a preferential uptake orientation towards the interface because the carbonyl-O atom has a strong interaction with interfacial H_2O. The uptakes and

* Corresponding author. Guangdong Key Laboratory of Environmental Catalysis and Health Risk Control, Guangdong-Hong Kong-Macao Joint Laboratory for Contaminants Exposure and Health, Institute of Environmental Health and Pollution Control, Guangdong University of Technology, Guangzhou, 510006, China.
E-mail address: jiym@gdut.edu.cn (Y. Ji).

https://doi.org/10.1016/j.atmosenv.2024.120859
Received 18 June 2024; Received in revised form 26 September 2024; Accepted 6 October 2024
Available online 9 October 2024

accumulations of MG and BA at the interfaces are promoted by the acidic condition. Subsequent interfacial hydrations of MG and BA in the acidic droplet are beneficial to yield diols, which can engage in oligomerization in the droplet interior to contribute SOA formation. Our results provide the theoretical insight into the interfacial chemistry of SαDs and their role in SOA formation.

1. Introduction

Atmospheric aerosol particles profoundly affect the global climate, visibility, and human health (Xiang et al., 2023; Zhang et al., 2015). Secondary organic aerosol (SOA), accounting for a large fraction of atmospheric aerosol particles, is mainly originated from the atmospheric oxidation of biological and anthropogenic volatile organic compounds (VOCs) (Hu et al., 2017; Li et al., 2023; Srivastava et al., 2022; Ying et al., 2015; Zheng et al., 2021), which yield various highly water-soluble organic carbonyls (Ji et al., 2017; Luo et al., 2019). Small α-dicarbonyls (SαDs), as a kind of typical and important organic carbonyls, contribute to more than 16% of SOA mass in the Pearl River Delta region (Ling et al., 2020) and in the Beijing-Tianjin-Hebei region (Li et al., 2021a), with the concentration in urban fogs, clouds, and mists up to hundreds of micromoles per liter (Faust et al., 1996; Jang et al., 2005; Munger et al., 1990). In addition, a modeling study also shows that SαDs contribute to 11 Tg C a^{-1} of SOA global source (Fu et al., 2008).

Abundant evidences reveal that the aqueous-phase reactions of SαDs contribute to the formation of SOA and brown carbon (BrC) (De Haan et al., 2017; Grace et al., 2020; Li et al., 2021b; Marrero-Ortiz et al., 2019; McNeill, 2015). The heterogeneous reactions of SαDs include aqueous oxidation, hydration, self-oligomerization, and acid-catalyzed reactions in cloudwater and the aqueous aerosol (McNeill, 2015). However, more and more studies show that the interfacial processes of aerosols such as reactive adsorption and photooxidation reaction play a promotional role in SOA formation (Ning et al., 2023; Sui et al., 2021; Zhang et al., 2019; Zhong et al., 2019b). Aerosol interface is believed as the first location for uptake and accommodation of atmospheric trace gases in the gas-to-particle allocation (De Haan et al., 2018; Martin-s-Costa et al., 2012; Tan et al., 2022; Zhong et al., 2019a). Therefore, more and more studies focus on the interfacial reactions of SαDs and their role in SOA formation (Kim et al., 2022; Sui et al., 2021; Wren et al., 2015; Zhu et al., 2020). Furthermore, a recent study has shown that the uptake of glyoxal is enhanced at the gas-liquid interface of the acidic droplet (Shi et al., 2020), which is related to the aerosol, cloud and fog droplets in real atmosphere. However, the effect of the acidic droplet interface on the uptake of SαDs is unclear, leading to the lack of systematically understanding about their physicochemical behavior in multiphase chemistry. Therefore, it is necessary to investigate the uptake of SαDs and their subsequent interfacial reactions in the neutral and acidic droplets.

In this study, the interfacial chemistry of the typical SαDs in the neutral and acidic droplets was investigated by combining classical molecular dynamics (CMD), Born-Oppenheimer molecular dynamics (BOMD) simulations and quantum chemical (QC) calculations. MG and biacetyl (BA) were chosen as the models of the typical SαDs because they have a high concentration up to parts-per-billion level in the polluted area (Qian et al., 2019; Xu et al., 2023). The kinetic and thermodynamic aspects of MG and BA were illustrated, including free energy profiles, molecular distributions, orientations, and adsorption and accommodation abilities. The effect of the acidity on the uptakes of MG and BA was discussed. The interfacial isomerizations and hydration reactions of MG and BA at the gas-liquid interfaces of the neutral and acidic droplets were studied, and the environmental implications in the atmospheric aerosol formation were also discussed.

2. Computational methods

2.1. Classical molecular dynamics simulations

All CMD simulations were performed using the NAMD software package (Phillips et al., 2005), and all dynamical configurations were visualized via the VMD software (Humphrey et al., 1996). The sub-3-nanometer particle is the critical size of the aerosol nucleation and growth (Kulmala et al., 2004), and the half size of the constructed droplet model is used to participate in the free-energy calculation. Considering the involved size in the free-energy calculation and the size of the nucleation particle, the models in the cube boxes of 4.0 × 4.0 × 4.0 nm^3 were constructed to describe the neutral and acidic droplets. The neutral droplet consisted of water molecules (H_2O). Considering that the concentration of sulfuric acid (SA) in the lower troposphere is in the range of 1–60 wt% (Curtius et al., 2001) and the atmospheric aerosol exhibits the moderate acidity (Pye et al., 2020), the SA solution with 40 wt% SA concentration is used to simulate the acidic droplet, which was composed of H_2O, hydronium ion (H_3O^+), bisulfate ion (HSO_4^-), and sulfate ion (SO_4^{2-}). The CMD calculation of the minimization and equilibrium was performed to guarantee the stability of droplets. Based on the above CMD results, the free-energy profiles of MG and BA migrating from the gas phase to the interior region of the droplets were obtained by using the umbrella sampling (Torrie and Valleau, 1977) and weighted histogram analysis methods (WHAM) (Kumar et al., 1992). The detailed description was shown in the Supporting Information (SI).

2.2. Born-Oppenheimer molecular dynamics simulations

All BOMD simulations based on the density functional theory method were performed using the CP2K software (Vande Vondele et al., 2005). The initial spherical model with the radius of 7.0 Å was constructed to emulate the droplet. The neutral droplet was composed of 48 H_2O, and the acidic droplet consisted of 5 SA and 37 H_2O. The above droplet models were initially placed in the periodic cubic box of 2.5 × 2.5 × 2.5 nm^3 to eliminate the interaction of adjacent repeat units. A pre-optimization of 5.0 ps at the timestep of 1.0 fs was implemented for each droplet model to ensure the system stability. Then MG and BA were randomly placed above the gas-liquid interface of the droplet and the whole systems were re-optimized for 10–15 ps. In order to clarify the reaction mechanisms of MG and BA at the gas-liquid interface, the free-energy barriers were calculated by the metadynamics (MTD) simulation using the PLUMED plug-in combined with the CP2K software (detailed description provided in the SI) (Barducci et al., 2011; Bonomi et al., 2009; Tribello et al., 2014).

2.3. Quantum chemical calculations

All QC calculations were performed via the Gaussian 09 program (Frisch et al., 2009), and the solvent model based on density was used to simulate the suitable solution condition (Marenich et al., 2009). The geometric optimizations of all stationary points (SPs), including the reactants, transition states (TSs) and products were carried out using the M06-2X functional (Zhao and Truhlar, 2008) with the 6–311++G(d,p) basis set, i.e., at the M06-2X/6–311++G(d,p) level. Frequencies were calculated at the same level to verify all SPs either as a real local minimum (without imaginary frequency) or a TS (with only one imaginary frequency). Intrinsic reaction coordinate (IRC) calculations were performed to confirm the connection between TSs and the corresponding

reactants and products. Based on the above geometries of all SPs, the single-point energies were further refined at the M06-2X/6–311++G (3df,3pd) level to yield more accurate potential surface energy (PES).

3. Results and discussion

There are two distinct processes in the whole migrations of MG and BA from the gas to the liquid phase, i.e., the gas-liquid interfacial adsorption (pathway I) and the subsequent reaction (pathway II) (Fig. S1). The pathway I involves the mutual attractions of gaseous MG and BA with the droplets and the uptakes of MG and BA at the gas-liquid interface. The pathway II corresponds to the hydration reactions of MG and BA at the gas-liquid interface which are the first steps of oligomerizations for SαDs (Gomez et al., 2015; Wren et al., 2015).

3.1. The mutual attractions of gaseous MG and BA with the droplets

The relative concentration distributions of MG and BA and the corresponding solvents along with the z-direction perpendicular to the interfaces are presented in Fig. S2. The interfacial widths are estimated to be 10.80 Å for the neutral droplet and 11.25 Å for the acidic droplet. In the whole migration, the relative concentration distributions of MG and BA are rapidly reduced to a local minimum at the gas-liquid interface and eventually plateau in the gas phase. It implies that both of MG and BA exhibit an interfacial preference and are thereby readily absorbed and accommodated at the gas-liquid interfaces of the neutral and acidic droplets.

To evaluate the favorable conformations of MG and BA at the gas-liquid interfaces, the time evolutions of the positions for the *trans* and *cis* conformations of MG and BA along with the z-direction perpendicular to the interfaces are simulated and displayed in Figs. 1 and S3. For MG system, the duration of the *trans*-conformation of MG (*trans*-MG) accounts for more than 78.5% of the total time evolution at the gas-liquid interfaces of the neutral and acidic droplets, which is larger than that of the *cis*-conformation of MG (*cis*-MG). Similarly, the *trans* configuration of BA is more favorable to accumulate at the interface than the *cis* configuration. Figs. 2 and S4 depict the free energy profiles of the trajectories for MG and BA traveling from the gas phase into the droplet interior, respectively. A larger decrease in the free energy of *trans*-MG/BA (>4.50/5.45 kcal mol^{-1}) relative to *cis*-MG/BA (>3.95/5.27 kcal mol^{-1}) occurs when MG or BA approaches the gas-liquid interfaces of the neutral and acidic droplets, indicating the thermodynamical feasibility to the interfacial adsorptions and accommodations of *trans*-MG and *trans*-BA.

At the gas-liquid interface of the acidic droplet, the decrease in the free energy is further deepened (Figs. 2 and S4), and the distributions of *trans*-MG and *trans*-BA are more than 91.2% of the total time evolution (Figs. 1 and S3). It implies that the gas-liquid interface of the acidic droplet displays a preferred uptake and accommodation for the *trans* configurations of MG and BA. Furthermore, analysis of the orientation of *trans*-BA shows that the interfacial interaction is initiated by the carbonyl-O atom (Fig. S5), which possesses a more negatively charged natural bond orbital characteristic (−0.590 e) than that of *trans*-MG (−0.581 e), indicating that the interfacial electric attraction is more pronounced for *trans*-BA than *trans*-MG (Fig. S6).

To further assess the distributions of the *trans* and *cis* configurations of MG and BA at the gas-liquid interfaces, the isomerization reactions between the *trans* and *cis* configurations in MG and BA systems are also investigated. Figs. 3 and S7 display the free energy profiles of the isomerization reactions of MG and BA at the gas-liquid interfaces of the neutral and acidic droplets, respectively, as a function of torsion angle (τ, detailed depiction in the SI) and the schematic diagrams of the corresponding structures. In the neutral droplet, the most stable structure for *trans*-MG appears at 0.60 ps. There is a maximum of the free energy with 5.18 kcal mol^{-1} at 3.03 ps, corresponding to the formation of the TS. Finally, *cis*-MG is formed at 3.33 ps, and the reaction reaches the equilibrium. However, the isomerization from *cis*-MG to *trans*-MG proceeds a low free-energy barrier of 2.75 kcal mol^{-1}. Similarly, in the acidic droplet, there is the free-energy barrier of 3.74 kcal mol^{-1} for the transformation from *trans*-MG to *cis*-MG, higher than that from *cis*-MG to *trans*-MG (2.68 kcal mol^{-1}). Combining with the previous theoretical result that the *trans* isomer is the energetically more favorable structural configuration at the interfacial region relative to the *cis* isomer (Zhu et al., 2020), our results imply that the transformation from *trans*-MG to *cis*-MG is thermodynamically unfavorable relative to that from *cis*-MG to *trans*-MG. Analogously, for the isomerization from *trans*-BA to *cis*-BA, the free-energy barriers are 6.38 and 4.51 kcal mol^{-1} at the gas-liquid interfaces of the neutral and acidic droplets, respectively, which are higher than those from *cis*-BA to *trans*-BA. In addition, the free-energy barrier for the isomerization of BA is higher than that for the isomerization of MG, which is attributed to the large steric hindrance effect of the methyl group in BA. As discussed above, *trans*-MG and *trans*-BA are the preferred structural configurations at the interfacial region of the droplet, and the gas-liquid interface of the acidic droplet exerts a catalytic effect on the isomerizations of MG and BA. Hence, in the following study, the uptakes and hydrations of *trans*-MG and *trans*-BA will be further investigated and discussed.

3.2. Uptakes of MG and BA at the gas-liquid interfaces

The typical snapshots of the trajectories for *trans*-MG and *trans*-BA are analyzed and displayed in Figs. S5 and S8. Herein, the configurations

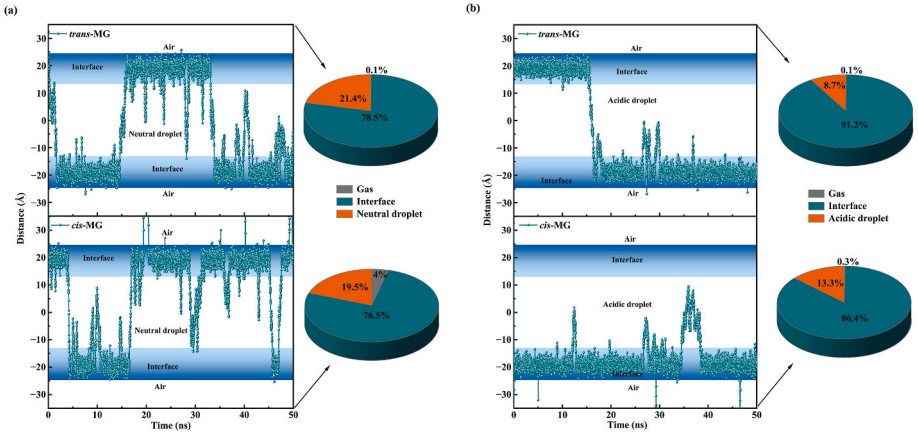

Fig. 1. The time evolutions of the positions and corresponding occurrence percentages of gaseous *trans*-MG and *cis*-MG along with the z-direction perpendicular to the gas-liquid interfaces of the (a) neutral and (b) acidic droplets.

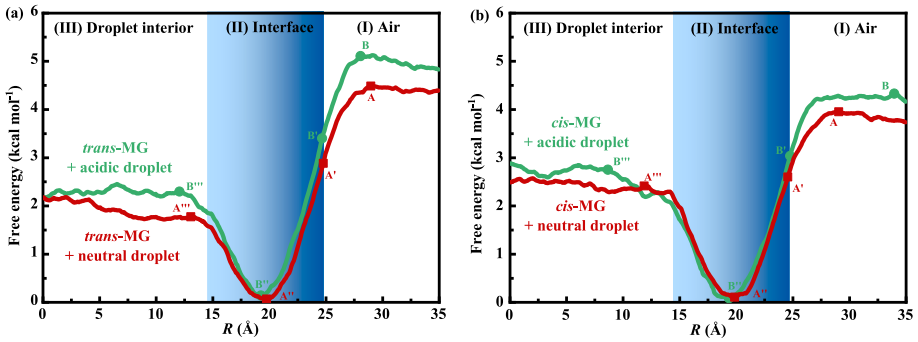

Fig. 2. The free energy profiles of gaseous (a) *trans*-MG and (b) *cis*-MG approaching the neutral and acidic droplets.

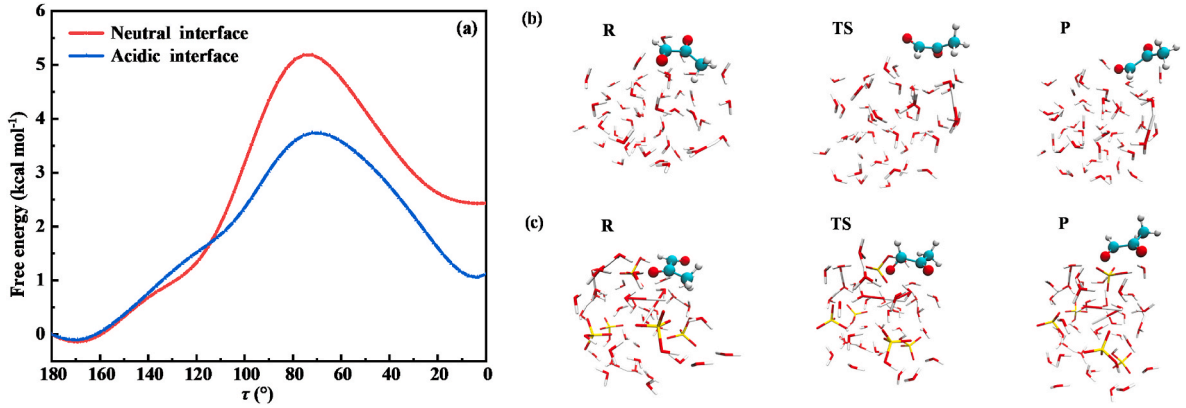

Fig. 3. (a) The free energy profiles for the isomerization from *trans*-MG ($\tau = 180°$) to *cis*-MG ($\tau = 0°$) at the gas-liquid interfaces of the neutral (red line) and acidic droplets (blue line); (b) and (c) represent the schematic diagrams of the reactants (Rs), TSs and products (Ps) at the gas-liquid interfaces of the neutral and acidic droplets, respectively.

A and B (Con A and B) denote the structures located at the free-energy maximum in the gas phase in the neutral and acidic droplets, respectively (point A and B in Figs. 2 and S4); the configurations A′ and B′ (Con A′ and B′) represent the snapshots on the boundaries between the gas phases and interfaces of the neutral and acidic droplets, respectively (point A′ and B′ in Figs. 2 and S4); the configurations A″ and B″ denote the

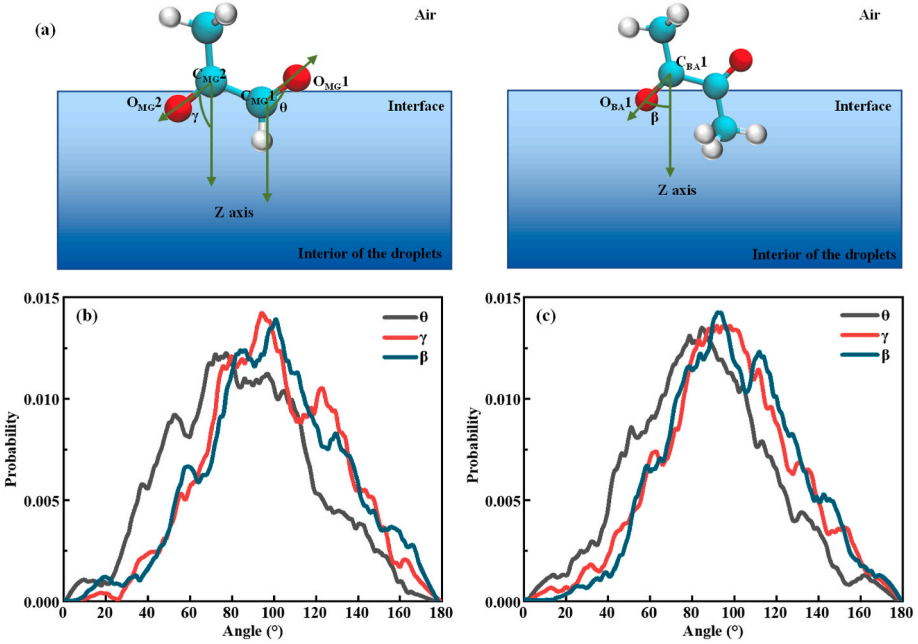

Fig. 4. Sketch for the angular coordinate. (a) θ and γ denote the angles between the z-axis and vector from $C_{MG}1$ to $O_{MG}1$ atoms and from $C_{MG}2$ to $O_{MG}2$ atoms in *trans*-MG; β represents the angle between the z-axis and vector from $C_{BA}1$ to $O_{BA}1$ atoms in *trans*-BA. The probability distributions of θ, γ, and β at the gas-liquid interfaces of the (b) neutral and (c) acidic droplets.

structures at the free-energy minimums at the interfaces of the neutral and acidic droplets, respectively (point A″ and B″ in Figs. 2 and S4). The configurations shown in Figs. S5 and S8 represent the most stable structures, corresponding to the total energy minimum at the corresponding window. As shown in Figs. S5 and S8, the carbonyl groups of *trans*-MG and *trans*-BA prefer to orient towards the gas-liquid interfaces of the neutral and acidic droplets, i.e., O atoms of the carbonyl groups closer to the interfaces.

To further identify the uptake orientation with respect to the interface, the angular distributions at the gas-liquid interfaces of the neutral and acidic droplets are calculated and showed in Fig. 4. For *trans*-MG, the angular distribution is described by θ and γ values, corresponding to the angles between z-direction with the aldehyde (θ) and ketone (γ) groups, respectively; for *trans*-BA, the angular distribution is depicted using β value, corresponding to the angle between z-direction with the ketone group. As shown in Fig. 4b and c, the θ and γ values at the gas-liquid interface of the neutral droplet are in the ranges of 65°–105° and 75°–105°, respectively; the corresponding values at the gas-liquid interface of the acidic droplet are in the ranges of 65°–105° and 75°–115°, respectively. The ranges of the β values at the gas-liquid interfaces of the neutral and acidic droplets are mainly located at 75°–115° and 75°–120°, respectively. It indicates that the C=O groups of *trans*-MG and *trans*-BA exhibit a preferential uptake orientation at both gas-liquid interfaces of the neutral and acidic droplets.

To further assess the role of the ions in the acidic droplet on the uptakes of MG and BA at the interfaces, hydrogen bonds (HBs) between MG and BA with the interfacial molecules are investigated, which are the key factor exhibiting the solvation effect at the interfacial regions. At the gas-liquid interface of the neutral droplet, there are two types of HBs for MG, i.e., the carbonyl-O atom with H atom of H_2O (denoted as $O_{MG}-H_{H2O}$) and the carbonyl-H atom with O atom of H_2O (represented as $H_{MG}-O_{H2O}$). For BA, only one type of HB exists, i.e., the carbonyl-O atom with H atom of H_2O ($O_{BA}-H_{H2O}$). The radial distribution functions ($g(r)$s) are used to depict the close interaction of two specific atoms and the peak intensity can illustrate the strength of the influence of the interfacial species. The radial distribution functions ($g(r)$s) of the above HBs are illustrated in Fig. 5a-c. Herein, we focus on the peak intensity for the $g(r)$s of HBs within 2.5 Å because the normal length of HB is from 1.50 Å to 2.38 Å (Zhao et al., 2009). No apparent peak of the $g(r)$ for $H_{MG}-O_{H2O}$ bond, while there is an obvious peak of the $g(r)$ for $O_{MG}-H_{H2O}$ or $O_{BA}-H_{H2O}$ bond, indicating a high probability for the formation of $O_{MG}-H_{H2O}$ or $O_{BA}-H_{H2O}$ bond at the gas-liquid interface. For the acidic droplet, except for the above $O_{MG}-H_{H2O}$ and $H_{MG}-O_{H2O}$ bonds for MG, there also exists other types of HBs, i.e., the carbonyl-O atoms with H atoms of H_3O^+ and HSO_4^- ($O_{MG}-H_{H3O+}$ and $O_{MG}-H_{HSO4-}$), and carbonyl-H atoms with O atoms of H_3O^+, HSO_4^-, and SO_4^{2-} ($H_{MG}-O_{H3O+}$, $H_{MG}-O_{HSO4-}$, $H_{MG}-O_{SO42-}$). No peak exists of the $g(r)$ for $H_{MG}-O_{H2O/-H3O+/HSO4-/SO42-}$ bond, while there is evident peak of the $g(r)$ for $O_{MG}-H_{H2O}$, $O_{MG}-H_{H3O+}$, or $O_{MG}-H_{HSO4-}$ bond. It indicates that H_3O^+ and HSO_4^- contribute to the uptake of MG at the interface of the acidic droplet. Furthermore, the peak intensity of the $g(r)$ for $O_{MG}-H_{H3O+}$ or $O_{MG}-H_{HSO4-}$ bond is weaker than that for $O_{MG}-H_{H2O}$ bond (Fig. 5c), implying more favorable formation of $O_{MG}-H_{H2O}$ bond in the acidic droplet. In addition, the higher peak of $O_{MG}-H_{H2O}$ bond in the acidic droplet relative to the neutral droplet indicates the stronger interaction between carbonyl-O atoms with H atoms of H_2O at the interface of the acidic droplet, which is attributed to the strong acidity provided by H_3O^+, HSO_4^- and SO_4^{2-}. Similarly, for BA, there are also HBs for the carbonyl-O atoms with H atoms of H_3O^+ and HSO_4^- ($O_{BA}-H_{H3O+}$ and $O_{MG}-H_{HSO4-}$). There exist also evident peaks of the $g(r)$ for $O_{BA}-H_{H2O}$, $O_{BA}-H_{H3O+}$, or $O_{BA}-H_{HSO4-}$ bond, and the peak intensity of the $g(r)$ for $O_{BA}-H_{H3O+}$ or $O_{BA}-H_{HSO4-}$ bond is also weaker than that of $O_{BA}-H_{H2O}$ bond (Fig. 5c). This implies that the uptakes and accommodations of MG and BA are promoted under the acidic condition with H_3O^+, HSO_4^-, and SO_4^{2-}.

3.3. Subsequent hydration reactions at the gas-liquid interfaces

Attack of *trans*-MG and *trans*-BA by the interfacial water yields diols (DLs). Figs. 6 and S9-S10 display the two-dimensional free-energy and the geometric diagrams of the key SPs in the hydration reactions. The time evolutions of key bond distances in the hydration reactions of *trans*-MG and *trans*-BA are showed in Figs. S11–S13.

For *trans*-MG at the gas-liquid interface of the neutral droplet, there are three steps in the hydration reaction for the aldehyde group (Fig. S11a): the HB formation via the first H-shift reaction, then the TS formation, and finally aldehyde-diol (ADL_{MG}) formation via the second H-shift reaction in the water cluster. For the first step (blue dashed arrow), the H atom ($H_{w1}1$) of the first water (W1) is shifted to the aldehyde-O atom of *trans*-MG ($O_{MG}1$) forming the HB ($H_{w1}1-O_{MG}1$) at

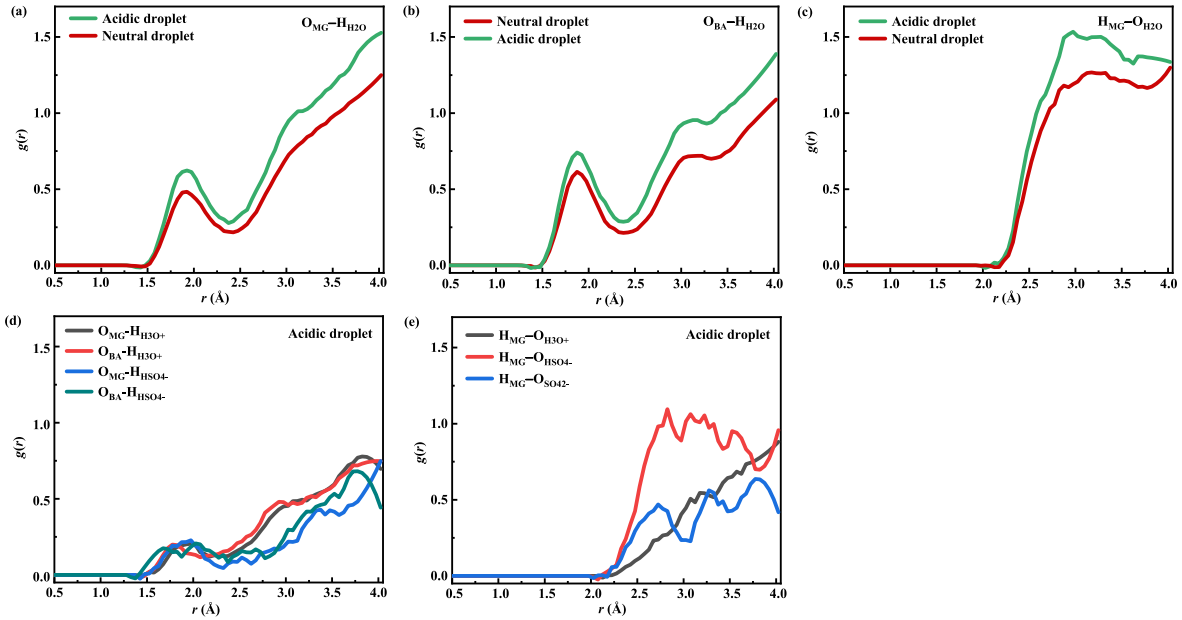

Fig. 5. Radial distribution functions ($g(r)$s) of (a) $O_{MG}-H_{H2O}$, (b) $O_{BA}-H_{H2O}$, (c) $H_{MG}-O_{H2O}$, (d) $O_{MG/BA}-H_{H3O+}$ and $O_{MG/BA}-H_{HSO4-}$, and (e) $H_{MG}-O_{H3O+/HSO4-/SO42-}$ at the gas-liquid interfaces of the neutral and acidic droplets.

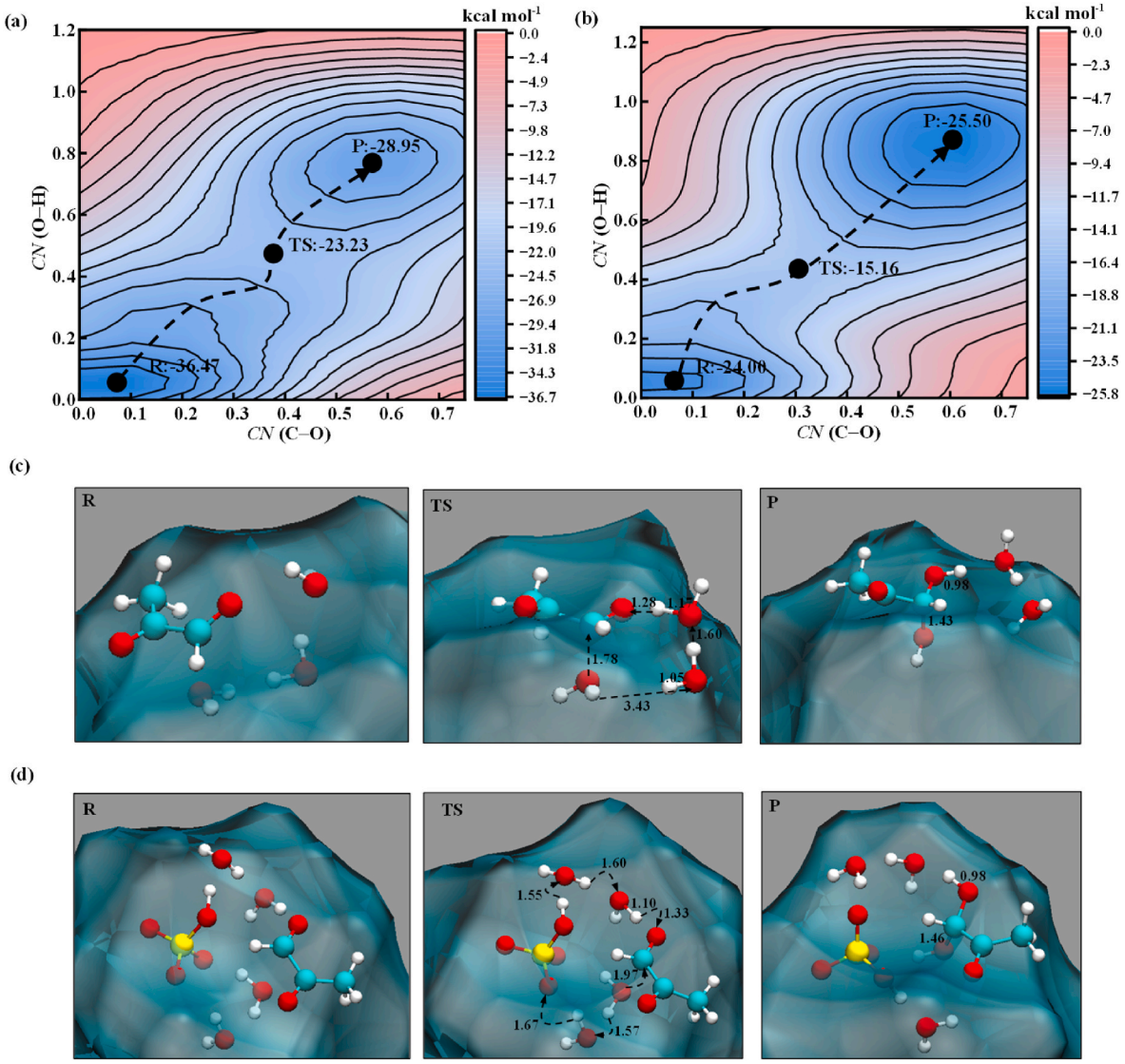

Fig. 6. (a) and (b) The free energy surface profiles in the hydration reactions for the aldehyde group of *trans*-MG at the gas-liquid interfaces of the neutral and acidic droplets; (c) and (d) the snapshot structures of the reactants (R), TSs, and products (Ps). The blue, white, red, and yellow spheres represent carbon, hydrogen, oxygen, and sulfur atoms, respectively.

5.82 ps, with the $H_{w1}1-O_{MG}1$ distance of 2.02 Å. Subsequently, the $H_{w1}1-O_{MG}1$ distance is gradually shortened but the $H_{w1}1-O_{w1}$ distance is elongated. The O atom (O_{w2}) of the second water (W2) approaches the carbonyl-C atom of *trans*-MG ($C_{MG}1$). For the second step (green dashed arrow), a maximum of the free energy with 13.24 kcal mol^{-1} is observed at 8.97 ps (Fig. 6a), corresponding to the formation of the TS. The lengths are 1.28 Å for $H_{w1}1-O_{MG}1$ bond and 1.78 Å for $C_{MG}1-O_{w2}$ bond, and the $H_{w1}1-O_{w1}$ bond is 1.17 Å (Fig. 6c). For the third step (brown dashed arrow), the H-shift reaction proceeds sequentially from W2 to the third water (W3), and then back to W1, yielding ADL_{MG} at 9.27 ps. Similarly, three steps also exist in the hydration reaction for the ketone group, to form ketone-diol (KDL_{MG}), with the free-energy barrier of 12.22 kcal mol^{-1} (detailed discussion in the SI and Fig. S12a). Hence, ADL_{MG} and KDL_{MG} are formed via the hydration reactions for the aldehyde and ketone groups of MG at the gas-liquid interface of the neutral droplet. In addition, our calculated free-energy barriers in the hydration reactions for the aldehyde and ketone groups of MG are only slightly different from those in a previous theoretical result (~10.0 and 12.5 kcal mol^{-1}), which obtained the free-energy barriers based on the QM/MM simulation (Zhu et al., 2020). The error in the free-energy barriers between our and previous theoretical results is as low as 2%, indicating that our calculation provides reliable data.

At the gas-liquid interface of the acidic droplet, there exist two mechanisms in the hydration reactions of MG: two steps without the participation of H_3O^+ (aldehyde group) and three steps with the participation of H_3O^+ (ketone group). For the aldehyde group, two steps in the hydration reaction are the TS formation (blue dashed arrow in Fig. S11b), and then ADL_{MG} and KDL_{MG} formation via the H-shift reaction (green dashed arrow in Fig. S11b). That is, the H atom of the first water ($H_{w1}1$) and the O atom (O_{w2}) of the second water (W2) at the gas-liquid interface gradually approaches the $O_{MG}1$ and $C_{MG}1$ atom of MG, respectively, to form the TS at 5.35 ps, corresponding to a free-energy maximum of 8.84 kcal mol^{-1}. Subsequently, the H-shift reaction occurs in a cluster that is composed of the bisulfate ion (HSO_4^-) and four water molecules. The lengths of $H_{w1}1-O_{MG}1$ and $C_{MG}1-O_{w2}$ bonds are shortened from 1.33 Å to 0.98 Å and from 1.97 Å to 1.46 Å at 5.76 ps, respectively, finally forming ADL_{MG}. For the ketone group, three steps in the hydration reaction correspond to the formation of cationic intermediate via the H-shift reaction from the hydronium ion (H_3O^+) to W1 and finally to O atom ($O_{MG}2$), then TS formation, and finally KDL_{MG} formation via the H-shift reaction between W2 and W3 (detailed discussion provided in the SI). Compared to the results in the neutral

droplet, the free-energy barriers of the hydration reactions for *trans*-MG in the acidic droplet are lower, indicating that the acidic condition facilitates the hydration reactions of MG at the gas-liquid interface.

Similar to those of *trans*-MG in the neutral droplet, three steps in the hydration reaction also exist for the ketone group of *trans*-BA at the gas-liquid interface (Fig. S13a). Firstly, the HB is formed via the $H_{w1}1$ atom shifted to the carbonyl-O atom ($O_{BA}1$), with the distance of 2.00 Å for $O_{BA}1-H_{w1}1$ bond at 7.29 ps (blue dashed arrow). Subsequently, the carbonyl-C atom ($C_{BA}1$) is attacked by O_{w2} atom to form a TS at 13.80 ps, with the free-energy barrier of 18.87 kcal mol^{-1} (green dashed arrow). Finally, the H-shift reaction within a three-water cluster is conducted, indicating the formation of ketone-diol (KDL_{BA}) (brown dashed arrow). However, at the gas-liquid interface of the acidic droplet, the hydration reaction of BA is also mediated by H_3O^+, and the first step is the formation of a cationic intermediate (CI) (blue dashed arrow in Fig. S13b), via the H-shift reaction between the hydronium ion (H_3O^+) and W1. The maximum of the free energy is 9.50 kcal mol^{-1} at 7.29 ps, which is lower than that in the neutral droplet, leading to the formation of KDL_{BA}. It indicates that the gas-liquid interface of the acidic droplet is also conductive to the hydration reactions of BA, which can be explained by the proton affinity (ΔPA) of H_2O in the aqueous phase (Ji et al., 2024; Mauney et al., 2017). Compared to the hydration reactions of MG, the higher free-energy barriers in BA system suggest that the hydration reaction at the gas-liquid interface is hindered by the existence of the methyl group in BA.

4. Conclusions and atmospheric implications

The interfacial chemistry of atmospheric trace gases plays a significant role in SOA formation (Shi et al., 2020; Sui et al., 2021; Wang et al., 2021). SαDs, as a typical type of atmospheric trace gases, contribute to at least 16% of SOA formation under haze condition (Li et al., 2013; Ling et al., 2020; Xing et al., 2019). However, most works focusing on the heterogenous reactions of SαDs in aqueous phase neglect their interfacial chemistry (Li et al., 2021b; Marrero-Ortiz et al., 2019; Shi et al., 2024). Hence, we performed CMD and BOMD simulations to investigate the gas-liquid interfacial chemistry of MG and BA in the neutral and acidic droplets. Our CMD results reveal that both *trans* and *cis* configurations of MG and BA are prone to absorb and accommodate at the gas-liquid interfaces of the neutral and acidic droplets. However, the gas-liquid interface of the acidic droplet exhibits a stronger ability to uptake and accommodate MG and BA, especially for their *trans* configurations. The carbonyl groups of MG and BA exhibit the preferential uptake orientation to the gas-liquid interfaces in the processes of gaseous MG and BA approaching into the interfaces. There is a strong interaction between carbonyl-O atoms of MG and BA with the interfacial H_2O because of their negative charges, which promote the uptakes of MG and BA to the gas-liquid interfaces of the neutral and acidic droplets, especially for the acidic droplet. The BOMD results show that the subsequent hydration reactions of MG and BA to form DLs at the gas-liquid interface are mediated by the interfacial H_2O in the neutral droplet but are mediated by the interfacial H_2O, H_3O^+, and HSO_4^- in the acidic droplet. The free-energy barriers are lower at the gas-liquid interface of the acidic droplet than the neutral droplet. Hence, the gas-liquid interface of the acidic droplet is more beneficial for the uptakes and subsequent hydration reactions of MG and BA.

To estimate the contribution of the interfacial chemistry of SαDs to SOA formation, we calculated the hydration reactions of DLs formed from MG and BA systems in the droplet interior. The PES of the corresponding hydration reaction pathways is displayed in Fig. S14. The H_2O-mediated hydration reactions of three DLs possess the large energy barriers with the range of 30.40–43.16 kcal mol^{-1}, while the proton-mediated hydration reactions of the above three DLs are barrierless and largely exothermic with the reaction energies less than −104.20 kcal mol^{-1}. It indicates that the proton-mediated hydration reactions of three target DLs are thermodynamically favorable to yield tetrols in the droplet interior. Hence, excessive formed DLs from MG and BA systems at the gas-liquid interface, which can enter into the droplet interior, engages in the oligomerization reactions, thereby accelerating the accommodations and yields of more DLs at the gas-liquid interfaces. The previous works focusing on the aqueous chemistry of SαDs such as glyoxal and MG show that carbenium ion-mediated oligomerizations of SαDs are the key mechanisms of SOA and BrC formation in the interior of the aerosol (Ji et al., 2020, 2022; Shi et al., 2024). However, these works are lack of the knowledge about reactive uptake process in gas-particle partitioning, while our current findings reveal the enhanced uptakes and hydration reactions of MG and BA at the gas-liquid interface of the acidic droplet, and also provide a theoretical insight into the interfacial chemistry of SαDs and their role in SOA formation.

CRediT authorship contribution statement

Qiuju Shi: Writing – review & editing, Writing – original draft, Validation, Investigation, Formal analysis, Data curation. **Ruize Ma:** Investigation, Formal analysis, Data curation. **Yongpeng Ji:** Writing – review & editing, Validation. **Weina Zhang:** Writing – review & editing, Validation. **Yuemeng Ji:** Writing – review & editing, Validation, Supervision. **Taicheng An:** Supervision.

Declaration of competing interest

The authors declare that they have no known competing financial interests or personal relationships that could have appeared to influence the work reported in this paper.

Data availability

Data will be made available on request.

Acknowledgements

This work was financially supported by National Natural Science Foundation of China (42077189 and 42020104001), Guangdong Basic and Applied Basic Research Foundation (2019B151502064), Local Innovative and Research Teams Project of Guangdong Pearl River Talents Program (2017BT01Z032), Science and Technology Key Project of Guangdong Province, China (2019B110206002), and Guangdong Provincial Key R&D Program (2022-GDUT-A0007).

Appendix A. Supplementary data

Supplementary data to this article can be found online at https://doi.org/10.1016/j.atmosenv.2024.120859.

References

Barducci, A., Bonomi, M., Parrinello, M., 2011. Metadynamics. WIREs Comput. Mol. Sci. 1, 826–843.
Bonomi, M., Branduardi, D., Bussi, G., et al., 2009. PLUMED: a portable plugin for free-energy calculations with molecular dynamics. Comput. Phys. Commun. 180, 1961–1972.
Curtius, J., Sierau, B., Arnold, F., et al., 2001. Measurement of aerosol sulfuric acid: 2. Pronounced layering in the free troposphere during the second Aerosol Characterization Experiment (ACE 2). J. Geophys. Res. Atmos. 106, 31975–31990.
De Haan, D.O., Hawkins, L.N., Welsh, H.G., et al., 2017. Brown carbon production in ammonium- or amine-containing aerosol particles by reactive uptake of methylglyoxal and photolytic cloud cycling. Environ. Sci. Technol. 51, 7458–7466.
De Haan, D.O., Jimenez, N.G., de Loera, A., et al., 2018. Methylglyoxal uptake coefficients on aqueous aerosol surfaces. J. Phys. Chem. A 122, 4854–4860.
Faust, B.C., Powell, K., Rao, C.J., et al., 1996. Aqueous-phase photolysis of biacetyl (an α-dicarbonyl compound): a sink for biacetyl, and a source of acetic acid, peroxyacetic acid, hydrogen peroxide, and the highly oxidizing acetylperoxyl radical in aqueous aerosols, fogs, and clouds. Atmos. Environ. 31, 497–510.
Frisch, M.J., Trucks, G.W., Schlegel, H.B., et al., 2009. Gaussian 09, Revision D.01. Gaussian, Inc., Wallingford CT.

Fu, T.M., Jacob, D.J., Wittrock, F., et al., 2008. Global budgets of atmospheric glyoxal and methylglyoxal, and implications for formation of secondary organic aerosols. J. Geophys. Res. 113, D15303.
Gomez, M.E., Lin, Y., Guo, S., et al., 2015. Heterogeneous chemistry of glyoxal on acidic solutions. An oligomerization pathway for secondary organic aerosol formation. J. Phys. Chem. A 119, 4457–4463.
Grace, D.N., Lugos, E.N., Ma, S., et al., 2020. Brown carbon formation potential of the biacetyl–ammonium sulfate reaction system. ACS Earth Space Chem. 4, 1104–1113.
Hu, J., Wang, P., Ying, Q., et al., 2017. Modeling biogenic and anthropogenic secondary organic aerosol in China. Atmos. Chem. Phys. 17, 77–92.
Humphrey, W., Dalke, A., Schulten, K., 1996. VMD: Visual molecular dynamics. J. Mol. Graph. 14, 33–38.
Jang, M., Czoschke, N.M., Northcro, A.L., 2005. Semiempirical model for organic aerosol growth by acid-catalyzed heterogeneous reactions of organic carbonyls. Environ. Sci. Technol. 39, 164–174.
Ji, Y., Luo, W., Shi, Q., et al., 2024. Mechanisms of isomerization and hydration reactions of typical β-diketone at the air-droplet interface. J. Environ. Sci. 141, 225–234.
Ji, Y., Shi, Q., Li, Y., et al., 2020. Carbenium ion-mediated oligomerization of methylglyoxal for secondary organic aerosol formation. Proc. Natl. Acad. Sci. U.S.A. 117, 13294–13299.
Ji, Y., Shi, Q., Ma, X., et al., 2022. Elucidating the critical oligomeric steps in secondary organic aerosol and brown carbon formation. Atmos. Chem. Phys. 22, 7259–7271.
Ji, Y., Zhao, J., Terazono, H., et al., 2017. Reassessing the atmospheric oxidation mechanism of toluene. Proc. Natl. Acad. Sci. U.S.A. 114, 8169–8174.
Kim, D., Cho, C., Jeong, S., et al., 2022. Field observational constraints on the controllers in glyoxal (CHOCHO) loss to aerosol. Atmos. Chem. Phys. 22, 805–821.
Kulmala, M., Pirjola, L., MaËkelaË, J.M., 2004. Stable sulphate clusters as a source of new atmospheric particles. Nature 404, 66–69.
Kumar, S., Bouzida, D., Swendsen, R.H., et al., 1992. The weighted histogram analysis method for free-energy calculations on biomolecules. I. The method. J. Comput. Chem. 13, 1011–1021.
Li, F., Tong, S., Zhang, W., et al., 2023. Characteristics of atmospheric non-methane hydrocarbon compounds (NMHCs) and their sources in urban typical secondary transformation in Beijing, China. Appl. Geochem. 155, 105732.
Li, J., Han, Z., Sun, Y., et al., 2021a. Chemical formation pathways of secondary organic aerosols in the Beijing-Tianjin-Hebei region in wintertime. Atmos. Environ. 244, 117996.
Li, N., Fu, T.M., Cao, J., et al., 2013. Sources of secondary organic aerosols in the Pearl River Delta region in fall: contributions from the aqueous reactive uptake of dicarbonyls. Atmos. Environ. 76, 200–207.
Li, Y., Ji, Y., Zhao, J., et al., 2021b. Unexpected oligomerization of small alpha-dicarbonyls for secondary organic aerosol and brown carbon formation. Environ. Sci. Technol. 55, 4430–4439.
Ling, Z., Xie, Q., Shao, M., et al., 2020. Formation and sink of glyoxal and methylglyoxal in a polluted subtropical environment: observation-based photochemical analysis and impact evaluation. Atmos. Chem. Phys. 20, 11451–11467.
Luo, H., Jia, L., Wan, Q., et al., 2019. Role of liquid water in the formation of O_3 and SOA particles from 1,2,3-trimethylbenzene. Atmos. Environ. 217, 116955.
Marenich, A.V., Cramer, C.J., Truhlar, D.G., 2009. Universal solvation model based on solute electron density and on a continuum model of the solvent defined by the bulk dielectric constant and atomic surface tensions. J. Phys. Chem. B 113, 6378–6396.
Marrero-Ortiz, W., Hu, M., Du, Z., et al., 2019. Formation and optical properties of brown carbon from small alpha-dicarbonyls and amines. Environ. Sci. Technol. 53, 117–126.
Martins-Costa, M.T.C., Anglada, J.M., Francisco, J.S., et al., 2012. Reactivity of volatile organic compounds at the surface of a water droplet. J. Am. Chem. Soc. 134, 11821–11827.
Mauney, D.T., Maner, J.A., Duncan, M.A., 2017. IR spectroscopy of protonated acetylacetone and its water clusters: enol–keto tautomers and ion→solvent proton transfer. J. Phys. Chem. A 121, 7059–7069.
McNeill, V.F., 2015. Aqueous organic chemistry in the atmosphere: sources and chemical processing of organic aerosols. Environ. Sci. Technol. 49, 1237–1244.
Munger, J.W., Jeff Collett, J., Bruce Daube, J., et al., 1990. Fogwater chemistry at riverside, California. Atmos. Environ. 24, 185–205.
Ning, A., Zhong, J., Li, L., et al., 2023. Chemical implications of rapid reactive absorption of I_2O_4 at the air-water interface. J. Am. Chem. Soc. 145, 10817–10825.
Phillips, J.C., Braun, R., Wei, W., et al., 2005. Scalable molecular dynamics with NAMD. J. Comput. Chem. 26, 1781–1802.
Pye, H.O.T., Nenes, A., Alexander, B., et al., 2020. The acidity of atmospheric particles and clouds. Atmos. Chem. Phys. 20, 4809–4888.
Qian, X., Shen, H., Chen, Z., 2019. Characterizing summer and winter carbonyl compounds in Beijing atmosphere. Atmos. Environ. 214, 116845.
Shi, Q., Gao, L., Li, W., et al., 2024. Oligomerization mechanism of methylglyoxal regulated by the methyl groups in reduced nitrogen species: implications for brown carbon formation. Environ. Sci. Technol. 58 (3), 1563–1576.
Shi, Q., Zhang, W., Ji, Y., et al., 2020. Enhanced uptake of glyoxal at the acidic nanoparticle interface: implications for secondary organic aerosol formation. Environ. Sci.: Nano 7, 1126–1135.
Srivastava, D., Vu, T.V., Tong, S., et al., 2022. Formation of secondary organic aerosols from anthropogenic precursors in laboratory studies. Npj Clim. Atmos. Sci. 5 (1), 22.
Sui, X., Xu, B., Yao, J., et al., 2021. New insights into secondary organic aerosol formation at the air-liquid interface. J. Phys. Chem. Lett. 12, 324–329.
Tan, S., Zhang, X., Lian, Y., et al., 2022. OH group orientation leads to organosulfate formation at the liquid aerosol surface. J. Am. Chem. Soc. 144, 16953–16964.
Torrie, G.M., Valleau, J.P., 1977. Nonphysical sampling distributions in Monte Carlo free-energy estimation: umbrella sampling. J. Comput. Phys. 23, 187–199.
Tribello, G.A., Bonomi, M., Branduardi, D., et al., 2014. Plumed 2: new feathers for an old bird. Comput. Phys. Commun. 185, 604–613.
Vande Vondele, J., Krack, M., Mohamed, F., et al., 2005. Quickstep: fast and accurate density functional calculations using a mixed Gaussian and plane waves approach. Comput. Phys. Commun. 167, 103–128.
Wang, X., Liu, S., Bao, L., et al., 2021. Enhanced uptake of methacrolein at the acidic nanoparticle interface: adsorption, heterogeneous reaction and impact for the secondary organic aerosol formation. Sci. Total Environ. 800, 149532.
Wren, S.N., Gordon, B.P., Valley, N.A., et al., 2015. Hydration, orientation, and conformation of methylglyoxal at the air-water interface. J. Phys. Chem. A 119, 6391–6403.
Xiang, W., Wang, W., Du, L., et al., 2023. Toxicological effects of secondary air pollutants. Chem. Res. Chin. Univ. 39, 326–341.
Xing, L., Wu, J., Elser, M., et al., 2019. Wintertime secondary organic aerosol formation in Beijing–Tianjin–Hebei (BTH): contributions of HONO sources and heterogeneous reactions. Atmos. Chem. Phys. 19, 2343–2359.
Xu, Y., Feng, X., Chen, Y., et al., 2023. Development of an enhanced method for atmospheric carbonyls and characterizing their roles in photochemistry in subtropical Hong Kong. Sci. Total Environ. 896, 165135.
Ying, Q., Li, J., Kota, S.H., 2015. Significant contributions of isoprene to summertime secondary organic aerosol in eastern United States. Environ. Sci. Technol. 49, 7834–7842.
Zhang, F., Yu, X., Sui, X., et al., 2019. Evolution of aqSOA from the air-liquid interfacial photochemistry of glyoxal and hydroxyl radicals. Environ. Sci. Technol. 53, 10236–10245.
Zhang, R., Wang, G., Guo, S., et al., 2015. Formation of urban fine particulate matter. Chem. Rev. 115, 3803–3855.
Zhao, J., Khalizov, A., Zhang, R., et al., 2009. Hydrogen-bonding interaction in molecular complexes and clusters of aerosol nucleation precursors. J. Phys. Chem. A 113, 680–689.
Zhao, Y., Truhlar, D.G., 2008. The M06 suite of density functionals for main group thermochemistry, thermochemical kinetics, noncovalent interactions, excited states, and transition elements: two new functionals and systematic testing of four M06-class functionals and 12 other functionals. Theor. Chem. Acc. 120, 215–241.
Zheng, Y., Chen, Q., Cheng, X., et al., 2021. Precursors and pathways leading to enhanced secondary organic aerosol formation during severe haze episodes. Environ. Sci. Technol. 55, 15680–15693.
Zhong, J., Kumar, M., Anglada, J.M., et al., 2019a. Atmospheric spectroscopy and photochemistry at environmental water interfaces. Annu. Rev. Phys. Chem. 70, 45–69.
Zhong, J., Li, H., Kumar, M., et al., 2019b. Mechanistic insight into the reaction of organic acids with SO_3 at the air–water interface. Angew. Chem. Int. Ed. 58, 8351–8355.
Zhu, C., Zeng, X.C., Francisco, J.S., et al., 2020. Hydration, solvation, and isomerization of methylglyoxal at the air/water interface: new mechanistic pathways. J. Am. Chem. Soc. 142, 5574–5582.